JOURNAL OF COMPUTATIONAL PHYSICS 75, 168–189 (1988)

A 3D Analysis of Maxwell's Equations for Cavities of Arbitrary Shape*

J. H. WHEALTON, G. L. CHEN, R. J. RARIDON,† R. W. MCGAFFEY,†
E. F. JAEGER, M. A. BELL,† AND D. J. HOFFMAN

Oak Ridge National Laboratory, Oak Ridge, Tennessee 37831

Received December 12, 1985; revised April 30, 1987

A three-dimensional analysis of cavity antennas is presented. The analysis is based on the finite difference method with a successive overrelaxation convergence scheme. This method permits the calculation of resonance frequencies and corresponding electric and magnetic fields of eigenmodes in cavity antennas with arbitrary shapes. © 1988 Academic Press, Inc.

I. INTRODUCTION

Cavity antennas have been used for various purposes, such as communication systems, for a long time. Recently, the usefulness of cavity antennas has aroused the interest of researchers in the plasma radio-frequency (rf) heating area, especially in the ion cyclotron resonance frequency (ICRF) range [1]. Ion cyclotron resonance heating (ICRH) has been successfully used for heating experiments in tokamaks and has been chosen to demonstrate ignition heating for next-generation tokamaks, such as the Tokamak Fusion Test Reactor (TFTR), the Joint European Torus (JET), and Doublet III. A carefully designed and fully tested resonant cavity antenna for these tokamaks is desirable. The Radio-Frequency Test Facility (RFTF) at the Oak Ridge National Laboratory (ORNL) is dedicated to this mission.

In designing a cavity antenna, it is necessary to understand its characteristic properties, such as resonant frequency, field components, impedance, etc. For a simple cavity, we can obtain these parameters by using the equivalent circuit method [2] or the variational principle method [3] or even by solving Maxwell's equations with analytical methods. However, these methods are very difficult or even impossible to apply to a complicated cavity such as those that are of interest for rf heating. Hence, we need to develop a three-dimensional (3D) analysis to

* Research sponsored by the Office of Fusion Energy, U.S. Department of Energy, under Contract DE-AC05-84OR21400 with Martin Marietta Energy Systems, Inc.

† Computing and Telecommunications Division, Martin Marietta Energy Systems, Inc.

0021-9991/88 $3.00

obtain a numerical solution of Maxwell's equations with complicated boundary conditions.

Numerical techniques have been developed to solve Maxwell's equations for boundaries of arbitrary shape. These techniques have a wide range of applications; examples include accelerator physics and the electromagnetic radiation and scattering problems [4]. Most of the techniques are designed to calculate the electromagnetic field from the sources, either charge density or current density. A good method for finding the resonance frequency and fields of eigenmodes is given by Hara *et al.* [4]. However, its accuracy becomes poor for very complicated boundary conditions, because the mesh size is limited by their finite element method. In general, the rf heating problem consists of analyzing the electromagnetic waves that couple a large number of eigenmodes together. Hence, finding an algorithm that solves for a large number of eigenmodes simultaneously and uses a reasonable amount of computer memory is very important for plasma heating theory.

Numerical techniques [5] that use the finite difference method combined with a relaxation convergence scheme to solve the wave equations for eigenvalue problems in a two-dimensional (2D) analysis have received considerable attention. In this work, we further investigate this technique in 3D cavities with boundaries of arbitrary shape. A finite difference analysis 3D Poisson equation [6] was developed by the authors for use in designing and conducting neutral beam experiments. We have extended this analysis to the 3D wave equation. Our analysis has several basic merits. First, a finite difference method [10] is used with a successive overrelaxation (SOR) convergence scheme and a method of treating boundaries that allows the cavity to have an arbitrary shape. Second, because of the SOR scheme, we need not find the inverse matrix to obtain the eigenvalue, which reduces the storage requirements. Third, either Dirichlet or Neumann boundary conditions are easily considered. Hence, more mesh points can be adopted for complicated boundary data or increased accuracy. Fourth, although our analysis is limited to the Cartesian coordinate system at present, a new scheme for treating the oblique boundary has been developed to allow cavities of arbitrary shape to exist in our problems. However, one of the disadvantages of SOR is the existence of convergence, and the convergence rates are strongly dependent on the chosen SOR factor. The third point implies that we can solve the wave equation in terms of **H** components as well as **E** components. Examining the Helmholtz magnetic field equation is important because it produces the lowest resonance frequency (see Section II), which is of considerable interest in ICRF plasma heating, where low-frequency launchers of compact dimensions are desirable.

The purpose of this paper is to demonstrate the analysis and its validity by calculating the eigenfrequencies and field components of a finite rectangular waveguide and other waveguides. The applications of this algorithm to rf heating will be given in a separate paper. The structure of the remainder of this paper is as follows. In Section II, we briefly describe the wave equations, boundary conditions, and possible constraining conditions. In Section III, we describe the subject analysis. Results for specific waveguides are presented in Section IV. We summarize

our conclusions in Section V. Appendix A gives the explicit form of the expansion coefficients used in Section II, and Appendix B gives a detailed discussion of the oblique boundary condition.

II. Wave Equations in Vacuum with Perfectly Conducting Walls

Since we consider the wave equations in vacuum, Maxwell's equations for the sinusoidal time-dependent $e^{-i\omega t}$ fields, **E** and **H**, are

$$\nabla \cdot \mathbf{H} = 0, \tag{1a}$$

$$\nabla \cdot \mathbf{H} = 0, \tag{1b}$$

$$\nabla \times \mathbf{E} = i\mu_0 \omega \mathbf{H}, \tag{1c}$$

$$\nabla \times \mathbf{H} = -i\varepsilon_0 \omega \mathbf{E}, \tag{1d}$$

where μ_0 and ε_0 are the permeability and dielectric constant in a vacuum. By combining the two curl equations and making use of the vanishing divergences, we find that both **E** and **H** satisfy

$$(\nabla + \mu_0 \varepsilon_0 \omega^2) \begin{Bmatrix} \mathbf{E} \\ \mathbf{H} \end{Bmatrix} = 0. \tag{2}$$

Boundary conditions on perfectly conducting walls are

$$\mathbf{n} \times \mathbf{E} = 0, \tag{3a}$$

$$\mathbf{n} \cdot \mathbf{H} = 0, \tag{3b}$$

where **n** is a unit vector outward normal to the surface of the boundary S. Equation (3) may be stated as follows: the boundary condition on **E** is that $E_{\|}$ vanish at the surface, and the boundary condition on **H** is that $\partial H_{\|}/\partial \mathbf{n}$ vanish at the surface, where $E_{\|}$ and $H_{\|}$ are the components of **E** and **H**, respectively, parallel to the boundary.

Equations (2) and (3) constitute the well-known eigenvalue problem. For the perfectly conducting cavity, all components of **E** and **H** are real. Equation (3) can be solved independently for three components. Since the boundary conditions on $E_{\|}$ and $H_{\|}$ are different, the corresponding eigenvalues will, in general, be different. For a simple eigenmode, there are three distinct categories of waves: transverse magnetic (TM) waves arise if the boundary condition is $E_{\|} = 0$, transverse electric (TE) waves arise if the boundary condition is $\partial H_{\|}/\partial \mathbf{n} = 0$. and transverse electromagnetic (TEM) waves arise if the boundary condition is $E_{\|} = 0$ and $H_{\|} = 0$. These three waves—TE, TM, and TEM—constitute a complete set of fields for

describing a cavity of arbitrary shape. In general, however, even for arbitrary shapes, analysis of an antenna requires only the study of some dominant modes. The lowest nontrivial eigenfrequency of the T mode is lower than that of the TM mode. For rf heating, a low-frequency, compact, high-power antenna is needed because of the typical port sizes and magnetic fields on tokamaks. Using plasma diagnostic techniques, the magnetic field can be directly measured by probe, but the absolute value of the electric field cannot be. Hence, solving Eq. (2) in terms of **H** is more practical, though it is sometimes more difficult.

For some eigenmodes, the eigenfunctions (**E** or **H**) are degenerate. When the eigenfunctions are degenerate, we impose conditions of constraint to remove the degeneracy. These constraint conditions could simply use Eq. (1a) or Eq. (1b).

III. Description of Analysis

A. *Convergence*

For simplicity, we discuss our numerical method in Cartesian coordinates. Thus, Eq. (2) can be rewritten in three scalar equations for H_x, H_y, and H_z:

$$\frac{\partial^2 H_x}{\partial x^2}+\frac{\partial^2 H_x}{\partial y^2}+\frac{\partial^2 H_x}{\partial z^2}+k^2 H_x=0, \tag{4a}$$

$$\frac{\partial^2 H_y}{\partial x^2}+\frac{\partial^2 H_y}{\partial y^2}+\frac{\partial^2 H_y}{\partial z^2}+k^2 H_y=0, \tag{4b}$$

$$\frac{\partial^2 H_z}{\partial x^2}+\frac{\partial^2 H_z}{\partial y^2}+\frac{\partial^2 H_z}{\partial z^2}+k^2 H_z=0, \tag{4c}$$

where $k^2=\mu_0\varepsilon_0\omega^2$. Similar equations can be obtained for **E** if we replace H by E in Eq. (4).

Equation (4) is similar to the Poisson equation with a linearized source term. We have modified the validated analysis described in Ref. [6] (which describes some of the details of this analysis). Here we expand the field (**E** or **H**) and its partial derivatives in Eq. (4) at node 0 (see Fig. 1) in terms of the fields at the node's neighbor grid points (1–6) by using the first-order finite difference approximation. We have, for example,

$$\begin{aligned} H_{z0} &= C_1 H_{z1}+C_2 H_{z2}+C_3 H_{z3}+C_4 H_{z4}+C_5 H_{z5}+C_6 H_{z6} \\ &= \sum_{i=1}^{6} C_i H_{zi}, \end{aligned} \tag{5}$$

where H_{zi} is the value of H_z at the ith node and C_i is the expansion coefficient in that direction. The detailed expressions for C_i are given in Appendix A.

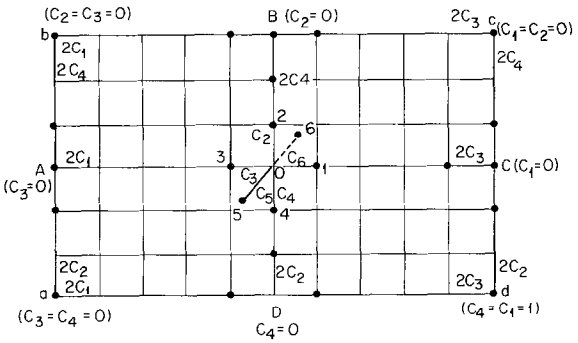

FIG. 1. The setup of nodal points and their finite difference expansion coefficients.

Then, we iterate the calculation by SOR until the difference between the two sides of Eq. (5) vanishes. That is, $\text{Res} = H_{z0} - \sum_i H_{zi} \approx 0$. This is defined as the minor iteration. During the minor iteration, k^2 is kept constant. Once H_j ($j = 1, 2, 3$, and $H_1 = H_x$, $H_2 = H_y$, $H_3 = H_z$) (or E_j) is found—that is, after a completed minor iteration—a new value of k^2 can be gotten from

$$k^2 = \left| \frac{-\nabla^2 H_j(u)}{H_j(u)} \right| \quad \text{or} \quad \left| \frac{-\nabla^2 E_j(u)}{E_j(u)} \right|, \tag{6}$$

where u is an arbitrarily chosen grid point, and H_j is normalized to $H_{j\max}$, which is the maximum value of all H_j. A major iteration is then finished. The new k^2 is input into another minor iteration. The iteration process is completed and the eigenfrequency is found when the previous k^2 and the latest k^2 are sufficiently close.

An alternative way to find the new k^2 needs to be mentioned here, because it converges rapidly in most cases. We can obtain the new k^2 by dividing k^2 by $H_{j\max}$ (or $E_{j\max}$) instead of computing from Eq. (6). Convergence is achieved when $H_{j\max}$ is close to unity. Mathematically, this corresponds to choosing the $J_j(u)$ equal to $H_{j\max}$ in Eq. (6). However, because the input H_j is close to the output H_j at this time, this method fails if the maximum value of H_j is assigned as a constant boundary value where the nodes are excluded from the iteration. The algorithm is shown in Fig. 2.

Convergence is critically dependent on the relaxation parameters [11] for the SOR method. In the major iteration, we use underrelaxation to get the new k^2 of the mth iteration; that is,

$$k_m^2 = \alpha k_m^2 + (1 - \alpha) k_{m-1}^2, \tag{7}$$

where k_m^2 is evaluated from Eq. (6). The underrelaxation parameter, α, is in the range $0 < \alpha \leqslant 1$. Similarly, we use overrelaxation with the relaxation parameter $1 \leqslant \beta < 2$ in the minor iteration; that is,

$$H_j^n = \beta H_j^n + (1 - \beta) H_j^{n-1}, \tag{8}$$

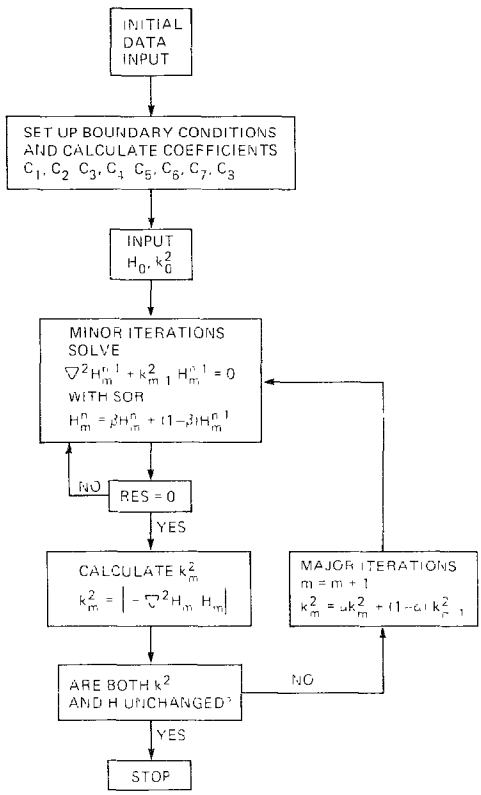

FIG. 2. Algorithm for Maxwell's equations.

where H_j^n is the result from Eq. (5). Whether or not the iteration process converges at all and whether the convergence is fast or slow depend on the chosen values of α and β. We give a more detailed discussion in Section IV. Theorems on the choice of α and β are being developed.

B. *Implementation of Boundary Conditions*

Either the Dirichlet boundary condition ($E_j = 0$ or $H_j = 0$) or the Neumann boundary condition ($\partial E_j/\partial x_k = 0$ or $\partial H_j/\partial x_k = 0$) is required to solve Eq. (4). For example, to solve Eq. (4c), we let $H_z = 0$ on boundary surfaces xy, $\partial H_z/\partial x = 0$ on boundary surfaces yz, and $\partial H_z/\partial y = 0$ on boundary surfaces zx, as illustrated in Fig. 3.

Two types of boundaries need to be discussed here: (a) a regular boundary and (b) an oblique boundary. Setting up the regular Dirichlet boundary condition is rather simple. We let the fields equal zero (or constant) only at the nodes and keep them constant on all iterations. The regular Neumann boundary condition should be satisfied when $\partial H_j/\partial x_k = 0$ at the boundary, where $j = 1, 2, 3$; $k = 1, 2, 3$; and

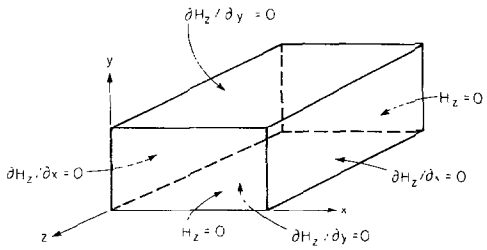

FIG. 3. Schematic representation of the cavity resonator and the boundary conditions of H_z.

$x_1 = x$, $x_2 = y$, and $x_3 = z$. For example, for the regular boundary illustrated in Fig. 4, we have

$$\left.\frac{\partial H_x}{\partial x}\right|_{x=0} \simeq \frac{H_{x1}h_3^2 - H_{x3}h_1^2 - H_{x0}(h_3^2 - h_1^2)}{h_1 h_3(h_1 + h_3)\,\Delta x}. \tag{9}$$

Equation (9) vanishes only if $h_1 = h_3$ and $H_{x1} = H_{x3}$. If we let $h_3 = h_1$ and $H_{x3} = H_{x1}$ in Eq. (A.5), we can see that only C_1 and C_3 are changed. They become $C_1 = 4h_1\lambda/\hat{L}$ and $C_3 = 0$. That is, C_1 is doubled and C_3 vanishes. Hence, to treat the regular Neumann boundary condition, we need to redefine the coefficients C_i and use the following rules. For a point that lies on the boundary line, C_i is set at zero for the direction that points outside the boundary, and the opposite C_i is doubled. For example, for point A, we let $C_3 = 0$ and double C_1; for point B, we let $C_2 = 0$ and double C_4; for point C, we let $C_1 = 0$ and double C_3; and for point D, we let $C_4 = 0$ and double C_2. For points that lie on the corners, we double the two non-zero C_i's that lie interior to the boundary. For example, for point a, we let $C_3 = C_4 = 0$ and double C_1 and C_2. The C_i's for points b, c, and d need similar treatment.

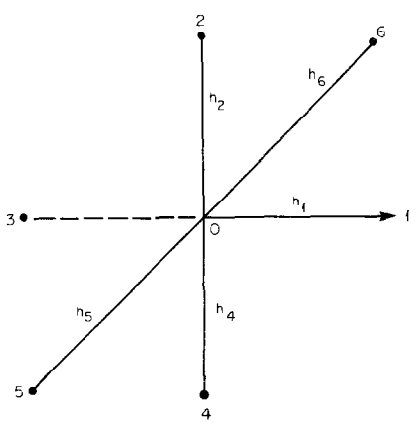

FIG. 4. Setting up the regular Dirichlet boundary condition.

We cannot expect all the boundaries to be fitted in the nodal lines. A typical case is shown in Fig. 5, a circle. This problem causes slight complications in the oblique Neumann boundary conditions. However, we have developed a new scheme [12] to deal with these oblique Neumann boundary conditions. The details of setting up the oblique boundary condition are given in Appendix B.

C. *Imposed Conditions for Higher Eigenmodes*

The procedure described in Section III.A can produce only the lowest mode, because Eq. (6) provides a bound only for the lowest eigenfrequency. It is worth pointing out here that the lowest eigenfrequency of the TE mode is zero, and the corresponding eigenfunction is an arbitrary constant. For this particular case, we can simply obtain the first nontrivial eigenfrequency by subtracting a constant from H_j (or E_j). This constant could be the averaged value of H_j (or E_j) at each iteration.

To obtain the nontrivial higher modes, we need to use the orthogonal properties of the eigenmodes [13], $H_n \cdot H_m = 0$ if $n \neq m$. Once we have determined the first mode, H_1, we can use $H^n - bH_1$ for the next stage of the iteration, where b is chosen to satisfy

$$H_1^*(H^n - bH_1) = 0. \tag{10}$$

Here H_1^* is the complex conjugate of H_1 and H^n is the value of H at the nth iteration. The second mode is then

$$H_2 = H^n - bH_1, \tag{11}$$

where H^n is the convergent value. After the second mode has been determined, $H^n - bH_1 - cH_2$ is used for the next stage of the iteration, with b and c chosen to satisfy

$$H_1^*(H_3^n - bH_1 - cH_2) = 0, \tag{12}$$

$$H_2^*(H_3^n - bH_1 - cH_2) = 0. \tag{13}$$

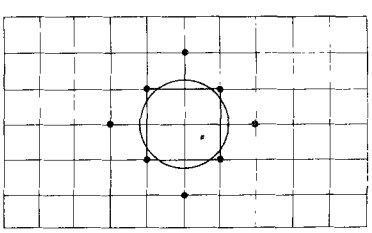

FIG. 5. A typical irregular boundary.

At convergence, the third mode will be

$$H_3 = H_3^n - bH_1 - cH_2. \tag{14}$$

This procedure is repeated until all of the desired modes have been obtained. The degenerate modes can also be determined with this procedure.

IV. Examples

We use a rectangular cavity, a ridge waveguide, and two complicated cavities to examine the validity of our analysis.

It is well known that if a, b, and c are the dimensions of a rectangular cavity (Fig. 6(a)) and $c \geqslant a > b$, then the magnetic field and electric field of the TE_{101} mode (the lowest nontrivial mode) are

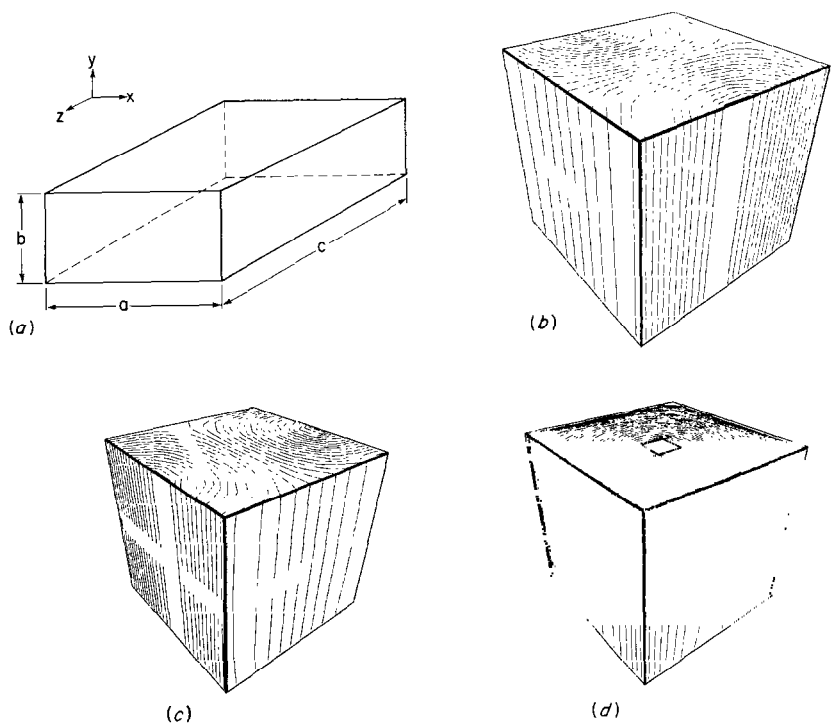

FIG. 6. Sample results for a resonant cavity: (a) dimensions of the cavity; (b) H_z of TE_{01} wave; (c) H_x of TE_{01} wave; (d) E_y of TE_{01} wave. The chained lines represent negative fields and the vector of field points to the inside of the paper.

$$H_x = A \sin \frac{\pi x}{a} \cos \frac{\pi z}{c}, \tag{15}$$

$$H_z = B \cos \frac{\pi x}{a} \sin \frac{\pi z}{c}, \tag{16}$$

$$E_y = C \sin \frac{\pi x}{a} \sin \frac{\pi z}{c}, \tag{17}$$

$$H_y = E_x = E_z = 0, \tag{18}$$

where A, B, and C are constants.

The corresponding eigenfunction is

$$k^2 = \frac{\pi^2}{a^2} + \frac{\pi^2}{c^2}. \tag{19}$$

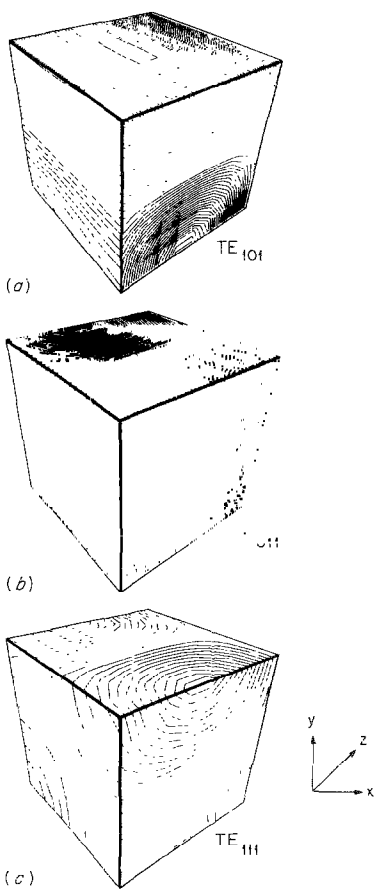

FIG. 7. The three lowest nontrivial TE modes of a rectangular cavity, obtained by the Gram–Schmidt method.

Figure 6 gives the results of our calculation with $a = c = 2m$ and $b = 1m$. In this paper, the contours of the field are plotted for all examples. The difference between the value of k^2 from the subject analysis ($=4.89\,\mathrm{m}^{-2}$) and that from Eq. (14) ($=\pi^2/2m^{-2}$) is less than 1%. Since the analysis of Section III considers arbitrary boundary data, and since the analysis cannot determine that the example of a shoebox cavity is solvable exactly, the agreement in the lowest eigenvalue constitutes a nontrivial validation of the subject analysis. The three lowest nontrivial TE modes (TE_{101}, Te_{011}, and TE_{111}) of a rectangular cavity with $a = 1.1$m, $b = 1$m, and $c = 1.2$m are obtained by the Gram–Schmidt orthogonalization method [13] and are shown in Fig. 7. The solutions of TE_{101} and TE_{011} reduce to the 2D results. This implies that our 3D algorithm can be used for 2D problems.

The second example considered is that of a ridged waveguide. This waveguide has a lower cutoff frequency and a wider band of useful frequencies than a rectangular waveguide with equivalent outside dimensions. Figure 8a shows a typical ridged waveguide and its lowest mode (TE_{01}) H_z field. Figure 8b shows the result for an infinitely long waveguide. Infinite length is a necessary assumption for the equivalent circuit approximation [2]. To compare our results with the equivalent

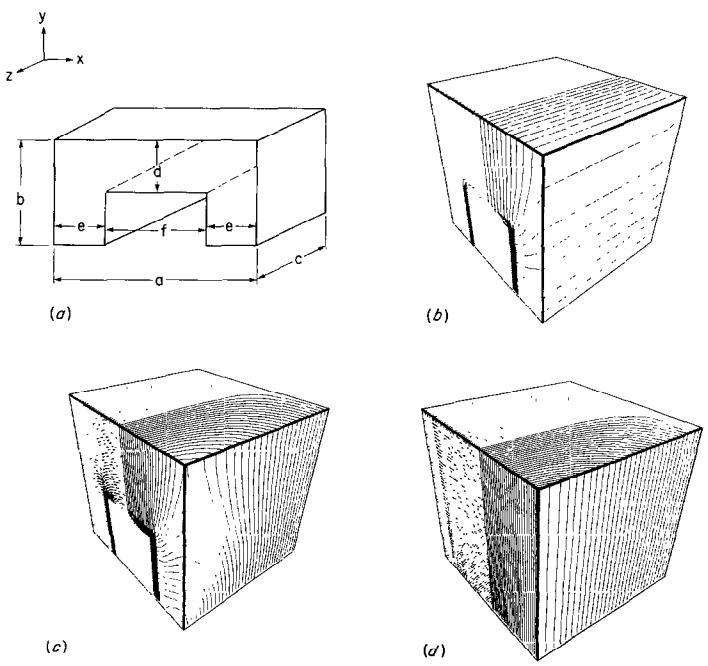

FIG. 8. Sample results for a ridged waveguide: (a) dimensions of the waveguide (a:b:d:$e = 4$:2:1:1); (b) H_z of TE_{01} wave for $c = \infty$ with both ends open; (c) H_z of TE_{01} wave for $c/b = 1$ with closed back end; (d) for comparison, H_z of TE_{01} wave for a rectangular waveguide with closed back end. The dashed lines represent negative fields and the vector of field points to the outside of the paper.

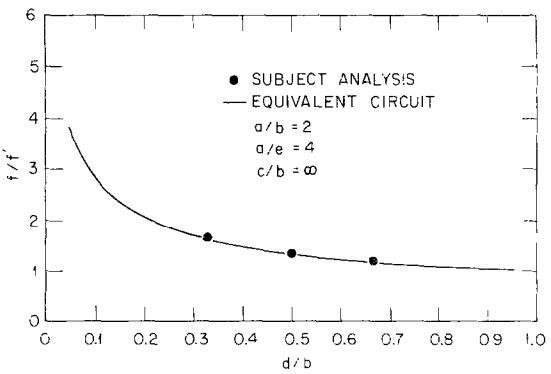

FIG. 9. Comparison of the eigenmode resonance frequencies computed with our method and with the equivalent circuit approximation by Pyle [2]. f/f' is the ratio of the resonant frequency with the rectangular waveguide to that with the ridged waveguide.

circuit approximation, the lowest eigenfrequencies of three ridged waveguides with different aspect ratios were computed by both methods. The results are plotted in Fig. 9 with apparent agreement. In order to illustrate our 3D analysis of the finite waveguide, Fig. 8c shows the results for a finite ridged waveguide ($c = b$), and Fig. 8d shows the results for a rectangular waveguide without the ridge. Both waveguides are closed by a metallic wall at the back end. The resonance frequency for the finite-length waveguide is reduced by only 13% due to the ridged effect. From Fig. 9, we find that the resonance frequency reduction is 28% for the corresponding infinitely long waveguides.

We also use this example to discuss the correlation of convergence and the relaxation parameters, α and β. For this purpose, two ridged waveguides with different aspect ratios (one infinitely long and the other with a finite length) have been used to study the convergence. The parameters for convergence are illustrated in Table I. For the infinitely long ridged waveguide, the result shows that convergence is speeded up with larger α and β if we keep the other parameters constant. In the case of the finite-length waveguide, closed only at one end with a Neumann boundary condition at the other end, the result shows that the code converges only at a particular parameter range. If the finite-length ridged waveguide is closed on both ends, then convergence is readily achieved for $0.05 < \beta \leqslant 1.7$, $0.05 < \alpha \leqslant 1$.

The third example of the analysis considered here is the cavity illustrated in Fig. 10a. This cavity is similar to the cavity antenna that has been proposed for the ICRH experiment in Doublet III-D [14]. Experiments on it are proceeding at the RFTF. Viewed from the side, the cavity is L-shaped. A vacuum cylinder (current strap), where the current flow enters the cavity, is located in the center of the vertical part of the L and is attached to a capacitor plate near the bottom of the L, where the current flows back.

TABLE I

The Parameters for Convergence for a Ridged Waveguide[a]

Aspect ratio	Minor iterations	β	a	Major iterations
$a=2, b=1, c=\infty$	45	1.0	1.0	64
			0.9	63
			0.8	72
			0.5	>100
	15	1.0	0.8	>100
		1.2		>100
		1.5		69
		1.7		34
$a=2, b=1, c=1$ (one end closed)	15	1.0	1.0	120
			0.7	80
			0.5	>120

[a] The number of nodes used here is $20 \times 18 \times 10$.

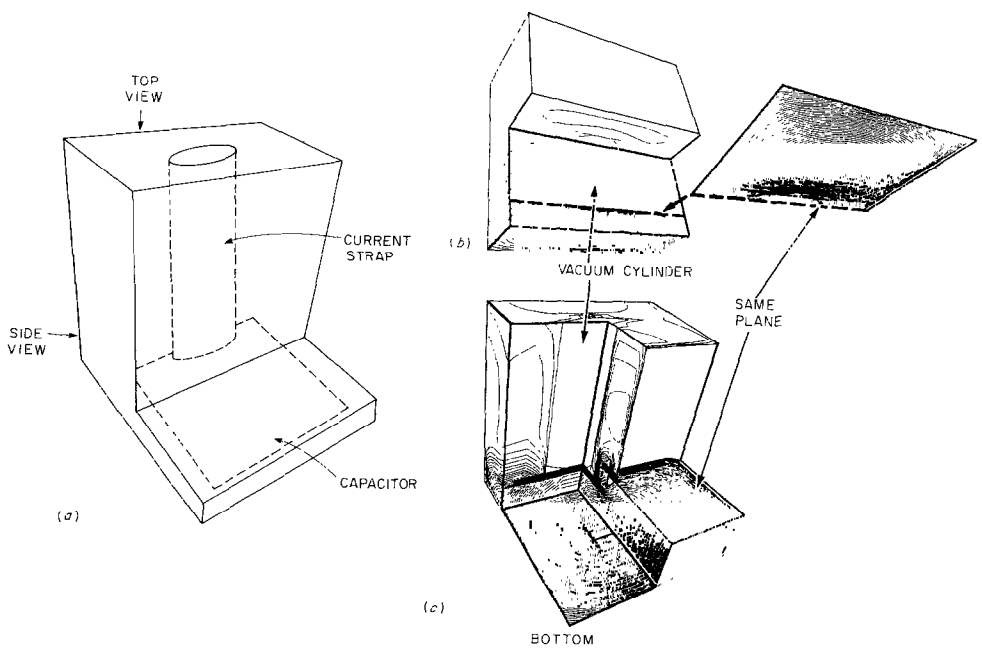

FIG. 10. Sample results for a complicated cavity: (a) structure of the cavity; (b) top view of $|E|$ field; (c) side view of $|E|$ field.

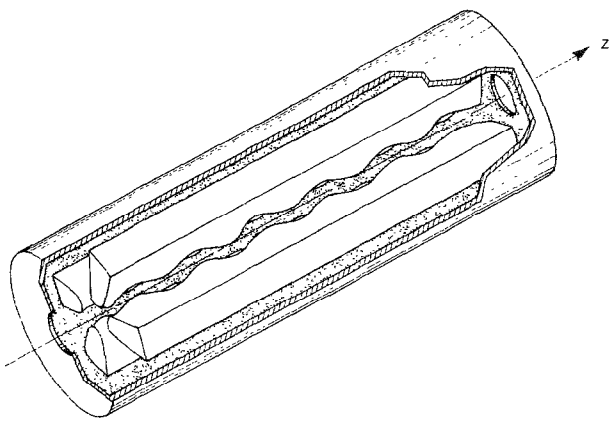

FIG. 11. Schematic of typical RFQ linear accelerator.

In our algorithm, the mesh points are located on cross-section planes; we cut as many of these planes as desired in one direction (the third direction). In this example, we examine the dependence of the results on the orientation of the mesh points. Figures 10b and 10c are cutaway views of the cavity in Fig. 10a that show contour plots of the electric field structure inside the cavity for the fundamental resonant mode. Figure 10b shows the results of a calculation in which the mesh points were set on planes cut parallel to the top of the cavity; these planes are rectangular with a circular hole (the vacuum cylinder). In Fig. 10c, the mesh points were set on planes cut parallel to the side of the cavity; these planes are L-shaped. The planes in Figs. 10b and c that are labeled "same plane" represent the outside surface of the cavity above the capacitor. It is easy to see that the two contour plots have the same pattern. The eigenfrequencies of both cases are identical to within 3%. This result proves that the subject analysis is independent of boundary data orientation.

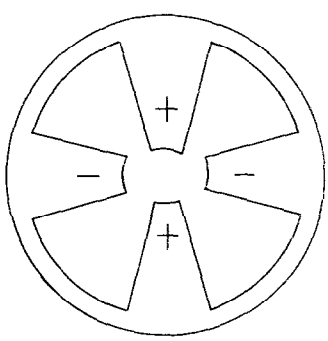

FIG. 12. Cross section of RFQ linear accelerator used in this example.

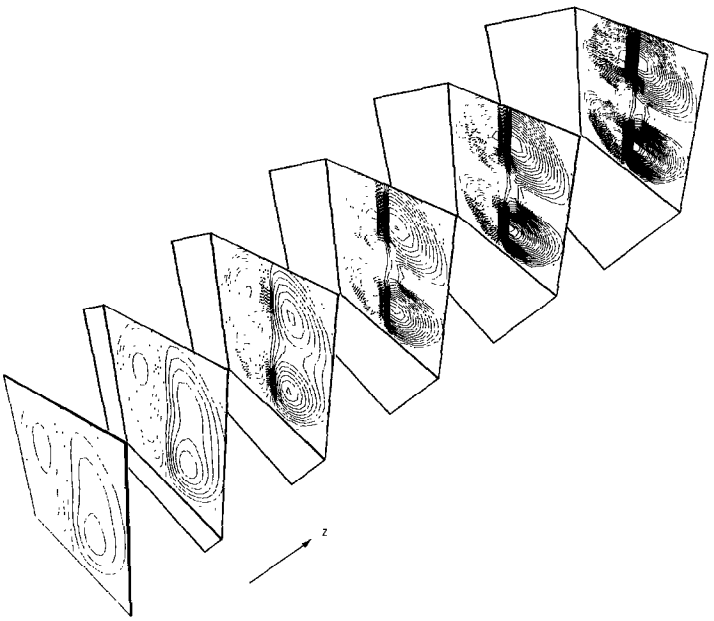

FIG. 13. Contour plots of E_γ at different cross sections through the accelerator.

For our final example, we apply our method to a radio-frequency quadrupole (RFQ) linear accelerator [15], shown in Figs. 11 and 12. The structure is excited so that the top and bottom vane tips are of one polarity, while the side vane tips are of the opposite polarity. The vane surfaces have considerable electric potential. There are gaps between the end plates and the vanes. Figure 13 is a series of contour plots of E_x at different cross sections through the accelerator. The plots show the transition between modes resulting from the 3D effect. The TE_{111} mode is dominant at the end plane, and the TE_{210} mode is dominant at the vanes.

V. SUMMARY

We have developed a 3D analysis that can deduce the resonance frequencies and the wave fields for a cavity antenna of arbitrary shape by using the finite difference method with an SOR convergence scheme. This analysis has been carefully tested for various cavities. The results are in good agreement with other theoretical analyses.

APPENDIX A. THE COEFFICIENTS OF C

From the finite difference approach (Taylor's theorem), we have

$$\frac{\partial H_{x0}}{\partial x} \simeq \frac{H_{x1}h_3^2 - H_{x3}h_1^2 - H_{x0}(h_3^2 - h_1^2)}{h_1 h_3(h_1 + h_3)\,\Delta x}, \tag{A.1a}$$

$$\frac{\partial^2 H_{x0}}{\partial x^2} \simeq 2\,\frac{H_{x1}h_3 + H_{x3}h_1 - H_{x0}(h_1 + h_3)}{h_1 h_3(h_1 + h_3)\,\Delta x^2}, \tag{A.1b}$$

$$\frac{\partial H_{x0}}{\partial y} \simeq \frac{H_{x2}h_4^2 - H_{x4}h_2^2 - H_{x0}(h_4^2 - h_2^2)}{h_2 h_4(h_2 + h_4)\,\Delta y}, \tag{A.1c}$$

$$\frac{\partial^2 H_{x0}}{\partial y^2} \simeq 2\,\frac{H_{x2}h_4 + H_{x4}h_2 - H_{x0}(h_2 + h_4)}{h_2 h_4(h_2 + h_4)\,\Delta y^2}, \tag{A.1d}$$

$$\frac{\partial H_{x0}}{\partial z} \simeq \frac{H_{x5}h_5^2 - H_{x0}(h_6^2 - h_5^2)}{h_5 h_6(h_5 + h_6)\,\Delta z}, \tag{A.1e}$$

$$\frac{\partial^2 H_{x0}}{\partial z^2} \simeq 2\,\frac{H_{x5}h_6 + H_{x6}h_5 - H_{x0}(h_5 + h_6)}{h_5 h_6(h_5 + h_6)\,\Delta z^2}, \tag{A.1f}$$

where Δx, Δy, and Δz are the uniform mesh intervals in the x, y, and z directions, respectively, and h_j (where $j = 1, 2, 3, 4, 5$ and 6) is the distance from point 0 to point j, normalized to Δx, Δy, or Δz. Substituting Eq. (A.1) into Eq. (4a) and defining

$$\lambda = \frac{1}{h_1 h_3(h_1 + h_3)\,\Delta x^2}, \tag{A.2}$$

$$\mu = \frac{1}{h_2 h_4(h_2 + h_4)\,\Delta y^2}, \tag{A.3}$$

$$\nu = \frac{1}{h_5 h_6(h_5 + h_6)\,\Delta z^2}, \tag{A.4}$$

and

$$\hat{L} = -2\left[\frac{1}{h_1 h_3 \Delta x^2} + \frac{1}{h_2 h_4 \Delta y^2} + \frac{1}{h_5 h_6 \Delta z^2} - k^2\right] \tag{A.5}$$

yields

$$2\lambda h_3 H_{x1} + 2\mu h_4 H_{x2} + 2\lambda h_1 H_{x3} + 2\mu h_2 H_{x4} + 2\nu h_6 H_{x5} + 2\nu h_5 H_{x6} - \hat{L} H_{x0} = 0. \quad \text{(A.6)}$$

Hence, we have

$$C_1 = 2h_3\lambda/\hat{L}, \quad \text{(A.7a)}$$

$$C_2 = 2h_4\mu/\hat{L}, \quad \text{(A.7b)}$$

$$C_3 = 2h_1\lambda/\hat{L}, \quad \text{(A.7c)}$$

$$C_4 = 2h_2\mu/\hat{L}, \quad \text{(A.7d)}$$

$$C_5 = 2h_6\nu/\hat{L}, \quad \text{(A.7e)}$$

$$C_6 = 2h_5\nu/\hat{L}. \quad \text{(A.7f)}$$

APPENDIX B. The Oblique Boundary Conditions

Setting up the oblique Dirichlet boundary condition is as simple as setting up the regular Dirichlet boundary condition. However, setting up the oblique Neumann boundary condition is quite complicated. The basic concept of the method [12] is to create a set of ghost points to achieve $\partial H/\partial n| = 0$ (or $\partial E/\partial n = 0$). Consider the four possible oblique boundaries we can have. They are shown in Fig. B.1. For

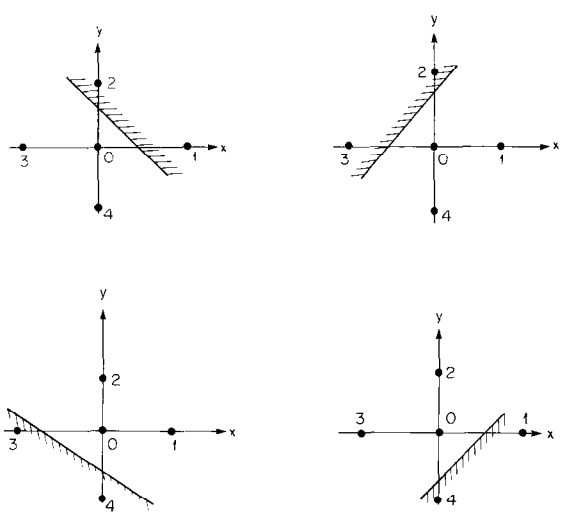

FIG. B.1. The four possible oblique boundaries.

uniformity, we must rotate the axes in Figs. B.1a, b, c, and d by 0°, -90°, -180°, and -270°, respectively. We characterize these rotation transform matrices as R_{90}:

$$\begin{pmatrix} 1 & 0 \\ 0 & 1 \end{pmatrix}, \quad \begin{pmatrix} 0 & -1 \\ 1 & 0 \end{pmatrix}, \quad \begin{pmatrix} -1 & 0 \\ 0 & -1 \end{pmatrix}, \quad \begin{pmatrix} 0 & 1 \\ -1 & 0 \end{pmatrix}.$$

After this procedure, we have the standard oblique boundary shown in Fig. B.2. The next step is to rotate the $x-y$ coordinate by an angle θ such that the oblique boundary can always be parallel to the y-axis. The matrix, R_θ, is

$$\begin{pmatrix} \cos\theta & -\sin\theta \\ \sin\theta & \cos\theta \end{pmatrix}.$$

Two ghost points, points 1′ and 2′ on Fig. B.3, are then created to cancel the parallel component field at points 3 and 4. The directions of those ghost vectors are determined by the following matrices G. For the case of Fig. B.1a,

$$G = \begin{bmatrix} 0 & 0 & 0 & 0 & 0 & 0 & 0 & 0 \\ 0 & 0 & 0 & 0 & 0 & 0 & 0 & 0 \\ 0 & 0 & 0 & 0 & 0 & 0 & 0 & 0 \\ 0 & 0 & 0 & 0 & 0 & 0 & 0 & 0 \\ 0 & 0 & 1 & 0 & 1 & 0 & 0 & 0 \\ 0 & 0 & 0 & -1 & 0 & 1 & 0 & 0 \\ 1 & 0 & 0 & 0 & 0 & 0 & 1 & 0 \\ 0 & -1 & 0 & 0 & 0 & 0 & 0 & 1 \end{bmatrix};$$

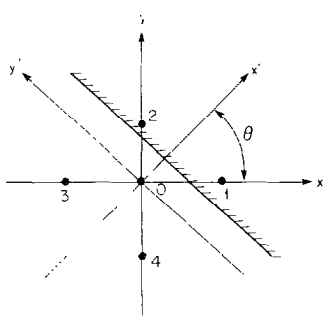

FIG. B.2. The standard oblique boundary.

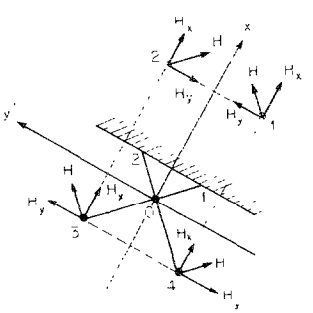

FIG. B.3. Locations of the ghost points.

for the case of Fig. B.1b,

$$G = \begin{bmatrix} 1 & 0 & 1 & 0 & 0 & 0 & 0 & 0 \\ 0 & 1 & 0 & -1 & 0 & 0 & 0 & 0 \\ 0 & 0 & 0 & 0 & 0 & 0 & 0 & 0 \\ 0 & 0 & 0 & 0 & 0 & 0 & 0 & 0 \\ 0 & 0 & 0 & 0 & 0 & 0 & 0 & 0 \\ 0 & 0 & 0 & 0 & 0 & 0 & 0 & 0 \\ 0 & 0 & 0 & 0 & 1 & 0 & 1 & 0 \\ 0 & 0 & 0 & 0 & 0 & -1 & 0 & 1 \end{bmatrix};$$

for the case of Fig. B.1c,

$$G = \begin{bmatrix} 1 & 0 & 0 & 0 & 0 & 0 & 1 & 0 \\ 0 & 1 & 0 & 0 & 0 & 0 & 0 & -1 \\ 0 & 0 & 1 & 0 & 1 & 0 & 0 & 0 \\ 0 & 0 & 0 & 1 & 0 & -1 & 0 & 0 \\ 0 & 0 & 0 & 0 & 0 & 0 & 0 & 0 \\ 0 & 0 & 0 & 0 & 0 & 0 & 0 & 0 \\ 0 & 0 & 0 & 0 & 0 & 0 & 0 & 0 \\ 0 & 0 & 0 & 0 & 0 & 0 & 0 & 0 \end{bmatrix};$$

and for the case of Fig. B.1d,

$$G = \begin{bmatrix} 0 & 0 & 0 & 0 & 0 & 0 & 0 & 0 \\ 0 & 0 & 0 & 0 & 0 & 0 & 0 & 0 \\ 1 & 0 & 1 & 0 & 0 & 0 & 0 & 0 \\ 0 & -1 & 0 & 1 & 0 & 0 & 0 & 0 \\ 0 & 0 & 0 & 0 & 1 & 0 & 1 & 0 \\ 0 & 0 & 0 & 0 & 0 & 1 & 0 & -1 \\ 0 & 0 & 0 & 0 & 0 & 0 & 0 & 0 \\ 0 & 0 & 0 & 0 & 0 & 0 & 0 & 0 \end{bmatrix}.$$

The magnitudes of the ghost vectors are determined by an 8×2 matrix,

$$A = \begin{bmatrix} A_1 & 0 \\ 0 & A_1 \\ A_2 & 0 \\ 0 & A_2 \\ A_3 & 0 \\ 0 & A_3 \\ A_4 & 0 \\ 0 & A_4 \end{bmatrix},$$

where A_1, A_2, A_3, and A_4 are the areas shown in Fig. B.4.

The last step is to rotate the coordinate system backward into the original system by matrices R_θ^{-1} and R_{90}^{-1}. Finally, we obtain the new coefficients for Eq. (5),

$$C' = \bar{R}_{90}\bar{R}_\theta G A R_\theta^{-1} R_{90}^{-1},$$

when $\bar{R}_{90}$ and $\bar{R}_\theta$ are the 8×8 matrices, with the 2×2 matrices, R_{90} and R_θ, placed along the diagonal, respectively. Hence, C' is an 8×2 matrix. The first column of elements of C' will contain the new coefficients of Eq. (5). (The second column of elements contains the coefficients for the complex field.) Equation (5) will be rewritten, in general, as

$$\begin{aligned} H_{j0} = {} & C'_1 H_{j1} + C'_2 H_{j2} + C'_3 H_{j3} + C'_4 H_{j4} + C'_5 H_{j5} + C'_6 H_{j6} \\ & + C'_7 H_{k1} + C'_8 H_{k2} + C'_9 H_{k3} + C'_{10} H_{k4}, \end{aligned}$$

where $k = j + 1$ if $j < 3$ and $k = j - 1$ if $j \geqslant 3$.

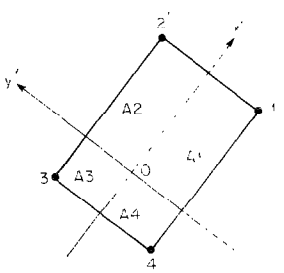

FIG. B.4. Areas used in calculating the magnitudes of the ghost vectors.

ACKNOWLEDGMENTS

The authors express their gratitude to D. H. Wooten for providing the interface between the subject analysis and the plotting routine, DISSPLA.

REFERENCES

1. For example, F. W. PERKINS AND R. F. KLUGE, *IEEE Trans. Plasma Sci.* **PS-12**, No. 2, 161 (1984).
2. J. R. PYLE, *IEEE Trans. Microwave Theory Tech.* **MTT-14**, No. 4, 175 (1966); S. B. COHN, *Proc. IRE* **35**, 783 (1948).
3. For example, J. SCHWINGER AND D. S. SAXON, *Discontinuities in Waveguides* (Gordon & Breach, New York, 1968).
4. M. HARA, T. WADA, T. FUKASAWA, AND F. KIKUCHI, *IEEE Trans. Nucl. Sci.* **NS-30**, 4, 3639 (1983); R. HOPPE, *Numer. Math.* **36**, 389 (1981); W. WILHELM, *Part. Accel.* **12**, 139 (1982); T. WEILAND, *Part. Accel.* **15**, 285 (1984); A. SANKER AND T. C. TONG, *Electron. Lett.* **11** (20), 481 (1975); J. J. H. WANG, *Radio Sci.* **13**, No. 6, 947 (1978); S. M. RAO, D. R. WILTON AND A. W. GLISSON, *IEEE Trans. Antennas Propag.* AP-30, No. 3, 409 (1982).
5. D. S. JONES, *Methods in Electromagnetic Wave Propagation* (Oxford University Press, Oxford, 1979); P. M. MORSE AND H. FESHBACH, *Methods of Theoretical Physics*, Vol. 1 (McGraw-Hill, New York, 1953), p. 696; R. F. HARRINGTON, *Field Computation by Moment Methods* (Macmillan Co., New York, 1968), p. 155; H. B. DAVIES AND C. A. MUILWYK, *Proc. IEE (London)* **113**, No. 2, 277 (1966).
6. J. H. WHEALTON, R. W. MCGAFFEY, AND P. S. MESZAROS, *J. Comput. Phys.* **63**, 20 (1986); J. H. WHEALTON, R. W. MCGAFFEY, AND P. S. MESZAROS, presented at the IEEE International Conference on Plasma Science, San Diego, 1983. The subject analysis derives from this Laplace equation 3D analysis which is validated in the third dimension by choosing a geometry that calibrates with respect to the second dimension. The Laplace equation (2D) analysis is described in Ref. [7] and validated by experiment in Ref. [8]. The 3D Helmholtz analysis herein or Ref. [9] derives directly from the analysis of Ref. [6].
7. J. H. WHEALTON, *Nucl. Instrum. Methods* **189**, 55 (1981); J. H. WHEALTON, *IEEE Trans. Nucl. Sci.* **NS-28**, 1358 (1981); J. H. WHEALTON AND J. C. WHITSON, *Part. Accel.* **10**, 235 (1980); J. H. WHEALTON, E. F. JAEGER, AND J. C. WHITSON, *J. Comput. Phys.* **27**, 32 (1978).
8. C. N. MEIXNER, M. M. MENON, C. C. TSAI, AND J. H. WHEALTON, *J. Appl. Phys.* **52**, 1167 (1981); J. H. WHEALTON, R. W. MCGAFFEY, AND W. L. STIRLING, *J. Appl. Phys.* **52**, 3787 (1981); J. KIM, J. H. WHEALTON, AND G. SCHILLING, *J. Appl. Phys.* **49**, 517 (1978); L. R. GRISHAM, C. C. TSAI, J. H. WHEALTON, AND W. L. STIRLING, *Rev. Sci. Instrum.* **48**, 1037 (1977); J. H. WHEALTON, *Bull. Amer. Phys. Soc.* **27**, 1136 (1982); J. H. WHEALTON, L. R. GRISHAM, C. C. TSAI, AND W. L. STIRLING, *J. Appl. Phys.* **49**, 3091 (1978); W. L. GARDNER *et al.*, *Rev. Sci. Instrum.* **52**, 1625 (1981); J. H. WHEALTON, R. J. RARIDON, R. W. MCGAFFEY, D. H. MCCOLLOUGH, W. L. STIRLING, AND W. K. DAGENHART, in *Proceedings. Third International Symposium on Production and Neutralization of Negative Ions and Beams, Brookhaven, 1983*, p. 524; W. L. STIRLING, W. K. DAGENHART, J. J. DONAGHY, AND J. H. WHEALTON, in *Proceedings, Third International Symposium on Production and Neutralization of Negative Ions and Beams, Brookhaven, 1983*, p. 450; J. H. WHEALTON, C. C. TSAI, W. K. DAGENHART, W. L. GARDNER, H. H. HASELTON, J. KIM, M. M. MENON, P. M. RYAN, D. E. SCHECHTER, AND W. L. STIRLING, *Appl. Phys. Lett.* **33**, 278 (1978).
9. J. H. WHEALTON, J. W. WOOTEN, R. W. MCGAFFEY, D. H. MCCOLLOUGH, R. J. RARIDON, M. A. BELL, P. S. MESZAROS, A. M. GOSWITZ, AND D. J. HOFFMAN, *Bull. Amer. Phys. Soc.* **28**, 1087 (1983).
10. J. S. HORNSBY, "A computer Programme for the Solution of Second Order Quasi-Linear Partial Differential Equations of the Elliptic Type Using the Method of Over-Relaxation," CERN-63-7 (European Organization for Nuclear Research, Geneva, 1963).

11. G. D. SMITH, *Numerical Solution of Partial Differential Equations: Finite Difference Methods*, 2nd ed. (Clarendon Press, Oxford, 1978).
12. R. W. MCGAFFEY, J. H. WHEALTON, R. J. RARIDON, J. W. WOOTEN, AND M. A. BELL, *Bull. Amer. Phys. Soc.* **29**, 146 (1984).
13. D. S. JONES, *Methods in Electromagnetic Wave Propagation*, p. 135 (Oxford University Press, Oxford, 1979).
14. D. J. HOFFMAN, F. W. BAITY, W. R. BECRAFT, J. B. O. CAUGHMAN, AND T. L. OWENS, *Fusion Technol.* **8**, No. 1, Pt. 2A, 411 (1985).
15. I. M. KAPCHINSKII AND W. V. LAZAREV, *IEEE Trans. Nucl. Sci.* **NS-26**, 3462 (1978).